*Int. J. Electrochem. Sci.*, 16 **(2021)** 150909, doi: 10.20964/2021.01.39

International Journal of
ELECTROCHEMICAL
SCIENCE
www.electrochemsci.org

*Short Communication*

# Effect of T4 and T6 Treatment on Electrochemical Corrosion Behavior of GW103K Magnesium Alloy

*Tao Jin*[1], *Shuang Yu*[2], *Shengzhi Liao*[1], *Ruiling Jia*[2,*], *Wen Ma*[2], *Feng Guo*[2]

[1] China Special Vehicle Research Institute, Aviation Key Laboratory of Science and Technology on Structural Corrosion Prevention and Control, Jingmen 448035, Hubei, P. R. China
[2] School of Materials Science and Engineering, Inner Mongolia University of Technology, Inner Mongolia Key Laboratory of Thin Film and Coatings Technology, Hohhot, 010051 PR China
[*]E-mail: jrl014014@163.com, jintao52020372@126.com

*Received:* 4 September 2020 / *Accepted:* 29 October 2020 / *Published:* 30 November 2020

GW103K (Mg-10Gd-3Y-0.4Zr) alloy can achieve better strength and elongation through precipitation hardening method. The precipitation sequence of the alloy has been identified as SSSS (cph)→β'' (D019) →β' (cbco)→β1(fcc)→β (bcc). In present work, the corrosion behavior was evaluated for the GW103K alloy under as-cast, solution treatment (T4) and aged treatment (T6) conditions，and the corrosion mechanism of the alloy after over-aging treatment (193h and 500h) was discussed. Electrochemistry impedance test results showed that the corrosion resistance of the alloy after T6-treated for 193h was the highest. The dissolution of $Mg_{24}(Gd,Y)_5$ phase led to severe localized corrosion on the as-cast alloy. The localized corrosion of the T4-treated alloy was inhabited because the micro-galvanic coupling between the $Mg_{24}(Gd,Y)_5$ phases and the matrix was reduced, which was attributed to the volume fraction of $Mg_{24}(Gd,Y)_5$ greatly decreased. Improved corrosion resistance of aged alloys could be attributed to the corrosion pits produced by the dissolution of the nano-scale β' phase were tiny and uniform, which led to the corrosion products on the surface more compact. However, slightly lower of corrosion resistance for the T6-500 h alloy was attributed to the spacing of the reticular structure of β' phase became wider and some of them transformed for β phase ($Mg_{24}(Gd,Y)_5$), the local corrosion was enhanced again.

**Keywords:** Mg alloy; over-aging treatment; corrosion； electrochemistry

## 1. INTRODUCTION

Mg-RE (rare earth) alloys have excellent properties and creep resistance at elevated temperature [1]. Especially the heavy RE elements, such as Gd and Y, can affect the precipitation kinetics and volume fraction of precipitates of Mg alloys. Mg-Gd-Y alloy is one of the most promising alloys in recent years [2, 3]. Heat treatment can change the structure and properties of Mg-RE alloys, which can possess the required mechanical strength, physical and chemical properties [4]. Solution (T4) and subsequent

artificial aging treatment (T6) are the main strengthening methods for most Mg-RE alloys [5]. Peng et al. [6] have found nearly continuous β'-network structure formed in Mg-10Gd-3Y-0.4Zr alloy after aging treatment, which acts as corrosion barrier and improve the corrosion resistance. Liang et al. [7] have also identified the continuous β' phase was generated in Mg-7Gd-3Y-0.4Zr alloy after aging treatment and the corrosion products is more uniform and compact than that of the as-cast alloy, so the corrosion resistance is improved. Wu et al. [8] have studied the corrosion behavior of Mg-10Gd-3Y-0.5Zr alloy in as-cast, solid solution and aging treatment. It is considered that the corrosion of as-cast alloy is related to the galvanic corrosion between the matrix and the eutectic compound. The improvement of corrosion resistance of the alloy after T4 treatment is attributed to the dissolution of the eutectic compound. These studies have shown that the proper heat treatment of Mg-Gd-Y alloy can improve the corrosion resistance significantly. In present, the study on corrosion resistance of Mg-Gd-Y alloy after heat treatment mainly focuses on the evolution of volume fraction of precipitates and the density and morphology of corrosion product caused by the content of Gd or Y. The effect of the type and size of precipitates on corrosion behavior of Mg-Gd-Y alloy after T6 treatment is not clear, especially the corrosion mechanism of the alloy after over-aging treatment is not well understand. In this paper, the authors reported a detailed study on the difference in the corrosion morphologies and dynamics of the GW103K alloy under as-cast, solid solution and over-aging treatment conditions.

## 2. EXPERIMENTAL

The composition of the GW103K alloy used in the present study was Mg-10.17wt.%Gd-3.24wt.%Y-0.35wt.%Zr, the alloy was developed by Light Alloy Net Forming National Engineering Research Center in Shanghai Jiao Tong University. The GW103K alloy specimens were subjected to subsequent heat treatment. The solution treatment (T4) was carried out at 500 ℃ for up to 4 h in an electric resistance furnace under the shelter of $CO_2$ and $SO_2$ gases which generated from the decomposition of mixed $CaCO_3$ and $FeS_2$. The specimens were quenched into hot water at 80 ± 3 ℃ to prevent the natural aging precipitation of supersaturated solid solution. Those specimens that had been subjected to solution treatment at 500 ℃ for 4 h then aged at 225 ℃ for 193 h and 500 h (T6), respectively. The specimens were also quenched in water at 80 ± 3 ℃ after T6 treatment.

Field emission scanning electron microscopy (FE-SEM, Sigma 500) was used to observe the microstructure of the GW103K alloy under different heat treatment conditions. Camera and Laser confocal microscopy (LSCM) were used to observe the corrosion morphologies on the surface of the specimens. Electrochemical atomic force microscopy (EC-AFM) was employed to observe the corrosion morphologies of the as-cast alloy and the T6-193h alloy in situ. The electrolyte in EC-AFM was 0.1 mol/L NaCl solution. The Pt wire was the counter electrode and the Cu wire was the reference electrode.

The electrochemical impedance measurements were carried out at Zennium electrochemical workstation produced by Zahner Company, in the frequency range from 1MHz to 10mHz, with a sinusoidal signal perturbation of 5mV. The reference electrode was a saturated calomel electrode (SCE), the counter electrode was a large area platinum plate. In order to prevent the corrosion product ($Mg(OH)_2$) produced during the test and changed the PH value of electrolyte solution, $Mg(OH)_2$ was added to 3.5 wt.% NaCl solution to form a saturated solution. The specimens of the GW103K alloy under different

heat treatment conditions were immersed in 3.5% NaCl solution at 25 ± 3 ℃ for 48 h before electrochemical impedance measurements.

## 3. RESULTS

Typical microstructures of the GW103K alloy observed under as-cast, T4 treatment and T6 treatment conditions are presented in Fig. 1. Optical micrographs can provide good contrast between the intermetallic phase and the α-Mg grains. The inserted images obtained by SEM show the shape and the quantity of the intermetallic phase. The as-cast alloy is characterized by an average grain size 50 μm and numerous intermetallic phase distributed along the dendrite boundaries (Fig. 1a). After T4 treatment, the grain structure with coarser grains of 70 μm is more homogeneous and the most of the intermetallic phase had dissolved, leaving a few refined skeleton-like phases and cuboid-shaped precipitates on the grain boundaries (Fig. 1b). The optical micrographs are similar for the specimens after aging for 193 h and 500 h. There are fine grains of 25 μm as well as coarse grains greater than 50 μm in the two alloys, the skeleton-like phases are precipitated again along the grain boundaries, but the amount of them reduced compared to that in the as-cast alloy. In our previous work [9], the skeleton-like phases have been recognized as $Mg_{24}(Gd,Y)_5$ phases.

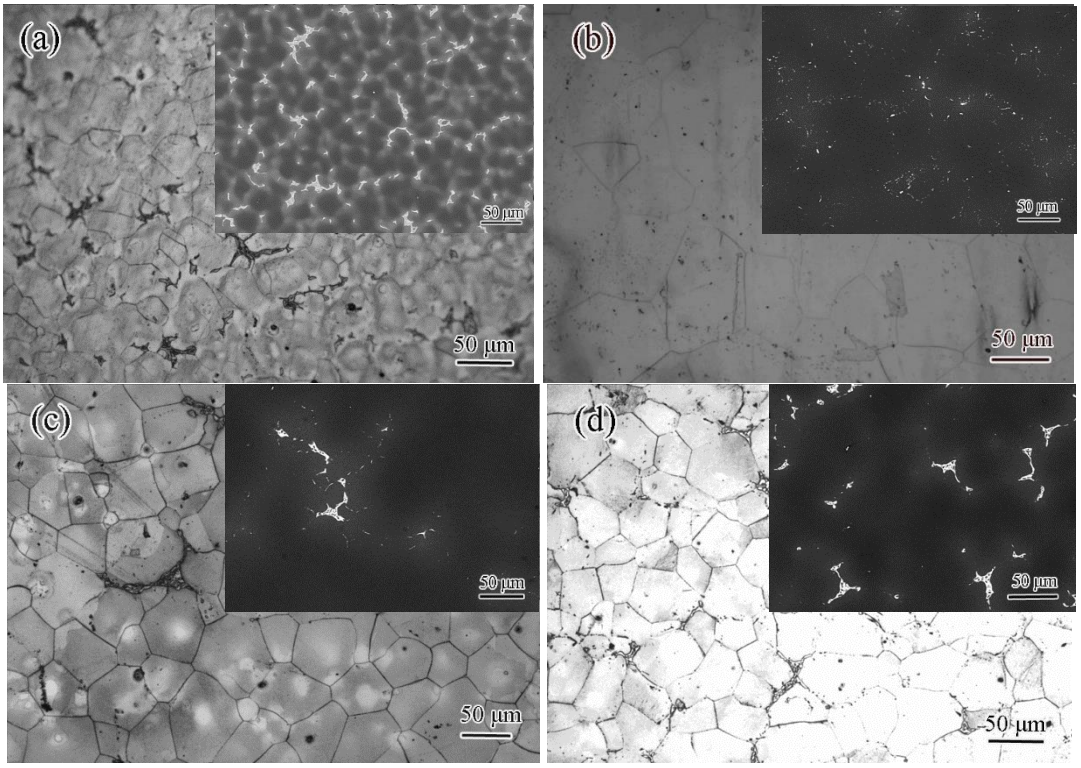


**Figure 1.** Optical and SEM micrographs of GW103K alloys: (a) as-cast alloy; (b) T4-treated alloy; (c) T6-193h alloy; (d) T6-500h alloy (inserts are SEM micrographs showing the structure of the intermetallic phases).

Fig. 2a shows the macro corrosion morphology of the as-cast alloy after immersed in 3.5% NaCl

solution for 48 h. The three-dimensional morphology of the pit (marked in Fig. 2a) is observed after magnified for 50 times by LSCM (shown in Fig. 2b), the area with the most severe corrosion is a dark blue region with a diameter of 0.2 mm, and the depth of which is about 2 mm. The α-Mg matrix with the pit as the center is also slightly corroded, and numerous pits with smaller diameter are scattered around the large one (marked in Fig. 2b). Fig. 2c shows the corrosion morphology of the as-cast alloy after immersed in 3.5% NaCl solution for 48 h, obviously, the corrosion of T4-treated alloy is much lighter than that of as-cast alloy, only a few corrosion pits appeared on the surface of the alloy. The three-dimensional morphology of the pit (marked in Fig. 2c) observed by LSCM (shown in Fig. 2d) show that the most severe corrosion is a dark blue region with a diameter of 0.2 mm, and the depth of which is about 1.2 mm. Figs. 2e and 2f show the corrosion morphologies and the three-dimensional morphology of the alloy after T6 treated for 193 h, respectively. Uniform corrosion of T6-193 h alloy can be observed from Figs. 2e and 2f, small pits appear on the surface of the alloy and the depth of the corrosion pits are about 200~300 μm. Figs. 2g and 2h show the corrosion morphologies and the three-dimensional morphology of LSCM for the alloy after T6 treated for 500 h, respectively. A corrosion pit has been seen on the surface of the alloy (square marked in Fig. 2g) and the most severe corrosion is a dark blue region with a diameter of 0.2 mm, and the depth of which is about 600 μm (shown in Fig. 2h). According to the microstructure of the T6-500h alloy，it is estimated that the pit is formed by the dissolution of $Mg_{24}(Gd,Y)_5$.

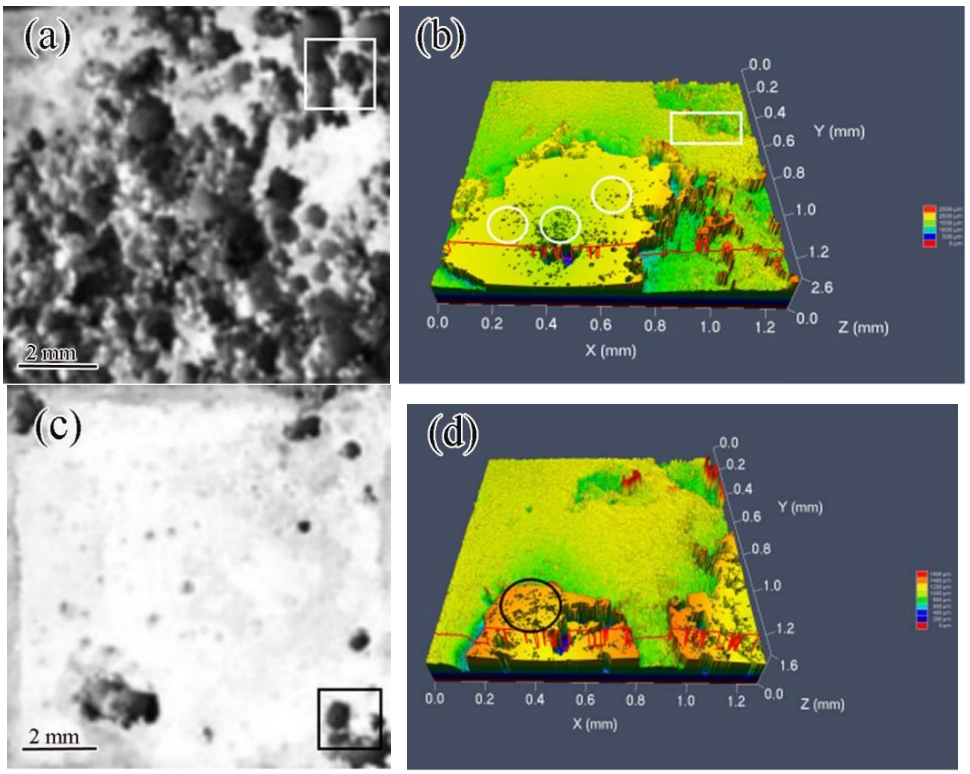

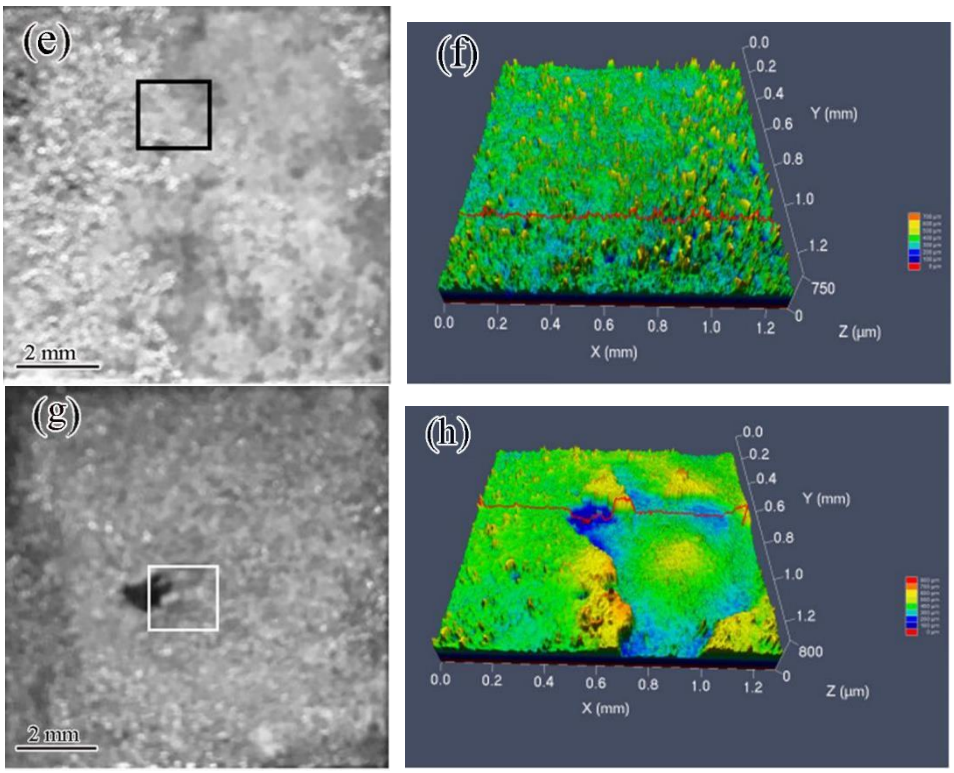


**Figure 2.** Macro corrosion morphology images by camera and three-dimensional height images of LSCM morphology images: (a) and (b): as-cast alloy; (c) and (d): T4-treated alloy; (e) and (f): T6-193h alloy; (g) and (h): T6-500h alloy

A series of in situ AFM images taken at different time intervals during immersion of the as-cast alloy and the T6-193h alloy in 0.1 mol/L NaCl solution is presented in Fig.3. It is found that the $Mg_{24}(Gd, Y)_5$ in the as-cast alloy is preferentially attacked (Fig.3a) and corrosion products become more and more with the increase of immersion time (marked in Fig.3b). The corrosion morphology on the surface of the T6-193 alloy is different from that of the as cast alloy. The observation that uniform corrosion products appeared after immersion for 40 min (Fig.3c) is consistent with the morphologies shown in Figs. 2e and 2f. When the immersion time reaches to 100 min, the part of loose corrosion products fell off, localized corrosion at the micron order can be noticed (squares marked in Fig.3d). In our previous work [9], it has been found that the β' phase can be precipitated in the alloy after T6 treatment and the corrosion behavior of the β' phase is characterized by dissolving preferentially, which results in tiny erect flaks corrosion products in the corrosion process. It is clear from the contrasting corrosion morphologies of the as-cast alloy and the T6-193h alloy that the amount of $Mg_{24}(Gd, Y)_5$ and β' phase is an important control factor for their corrosion behavior.

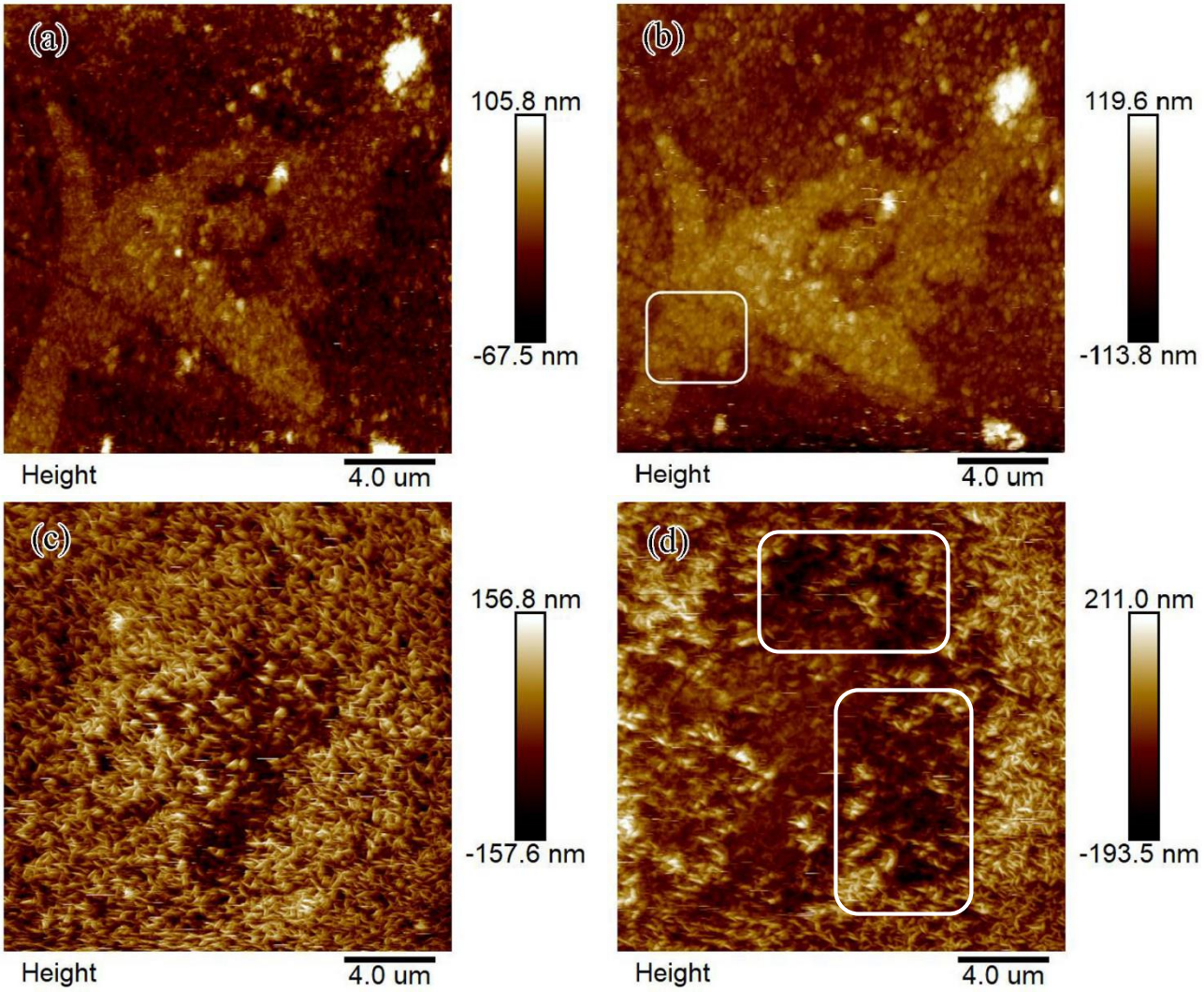


**Figure 3.** In situ corrosion morphologies under EC-AFM mode after immersion in 0.1 mol/L NaCl solution for different period: (a) 40 min; (b) 100 min for the as-cast alloy and (c) 40 min; (d) 100 min for the T6 -193 h alloy

The electrochemical impedance can obtain more kinetic and structure information of electrode interface [10]. The Nyquist plots of the as-cast alloy and the T4 treated alloy have consisted of one high frequency capacitance loop and two low frequency induction loops (Fig. 4a). The T6-treated alloy has a high frequency capacitance loop, a medium frequency capacitance loop, and a low frequency inductance loop. The Bode plots show that the impedance spectra contain at least two time constants of frequency vs. phase angle, namely, one wave crest and one wave trough. The different shapes of impedance spectra indicate the corrosion mechanism are different. The high frequency capacitance loop is associated with the electric double layer at the interface of matrix and electrolyte. The radius of capacitance loop represent the charge transfer resistance of the electric double layer. The medium frequency capacitance loop is attributed to mass transport in the solid phase. This is due to diffusion of ions to the metal surface from the electrolyte. The inductive behavior at low frequencies is generally associated with high concentration of Mg ions on relatively film-free areas or with an intermediate step in the corrosion process involving the presence of adsorbed surface species such as $Mg(OH)^{+}_{ads}$, $Mg(OH)^{2+}_{ads}$ and $Mg^{+}_{ads}$.

The short low frequency inductance loop should be attributed to the initiation of localized corrosion [11-13]. The shape of the high frequency capacitance loop of the alloy after T6 treated for 193 h is fuller, which means the dispersion effect is smaller and the corrosion product is more complete. The Nyquist plots of the as-cast alloy, T4-treated alloy and T6 treated for 500 h alloy showed obvious inductance, which indicates that the corrosion product is not compact enough and easy to crack locally at the later stage during the corrosion, which is a reason resulting in pitting corrosion [14].

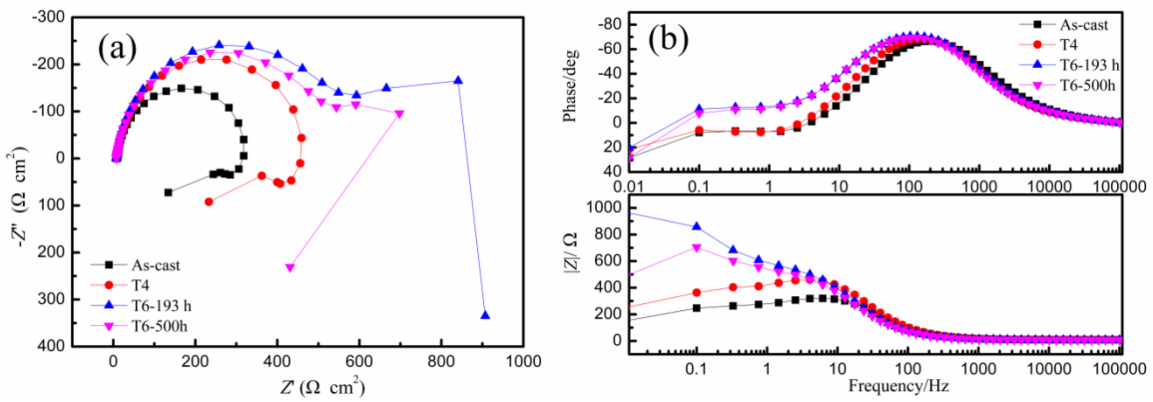


**Figure 4.** Electrochemical impedance spectra of GW103K alloy in 3.5% NaCl solution under different treatment condition: (a) Nyquist plots; (b) Bode plots.

**Table 1.** Fitting results of the EIS spectra of the as-cast alloy and the T4-treated alloy.

| Alloy | $R_{sol}$ /Ω.cm$^2$ | $CPE_{dl}$ /F.cm$^{-2}$ | $R_t$ /Ω.cm$^2$ | $n$ | $L_1$ /H | $R_1$ /Ω.cm$^2$ | $L_2$ /H | $R_2$ /Ω.cm$^2$ | Chsq |
|---|---|---|---|---|---|---|---|---|---|
| As-cast | 8.562 | $2.115\cdot10^{-5}$ | 296.5 | 0.9459 | $1.159\cdot10^{9}$ | 9.826 | $9.745\cdot10^{9}$ | $8.728\cdot10^{-9}$ | $7.41\cdot10^{-4}$ |
| T4 treated | 13.47 | $2.604\cdot10^{-6}$ | 427.8 | 0.9998 | 837.3 | 166 | $9.101\cdot10^{4}$ | $2.669\cdot10^{-2}$ | $7.07\cdot10^{-4}$ |

The impedance spectra of the as-cast and T4 treated alloys are fitted according to the equivalent circuit shown in Fig. 5. The corresponding parameters of each circuit element are listed in Table 1. $R_{sol}$ is the solution resistance, and $R_t$ is the charge transfer resistance. In order to avoid the error during the fitting, a constant potential element ($CPE$, $C_{dl}$) is selected to represent the capacitance of the electric double layer. $R_t$ and $C_{dl}$ together describe the first capacitance loop in high frequency. $L_1$ and $L_2$ are the inductances of the electrochemical reactions at the film/substrate interface; $R_1$ and $R_2$ are the resistances of the inductance, those used to describe low frequency inductance loops. The $R_t$ value increased of the T4-treated alloy elucidated the corrosion resistance is improved than that of the as-cast alloy. Fig. 6 is the experimental impedance and fitted curves based on the fitting circuit shown in Fig.5. The good agreement of them shows the rationality of the fitting results.

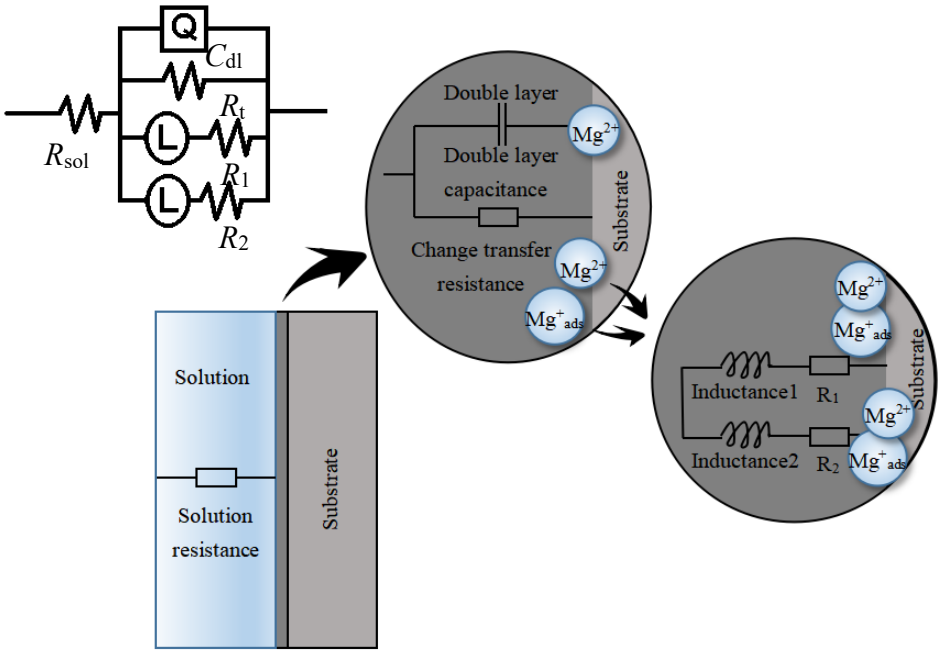


**Figure 5.** Equivalent circuit model of fitting EIS data and circuit model of physical properties of the film of corrosion products on the as-cast alloy and the T4-treated alloy.

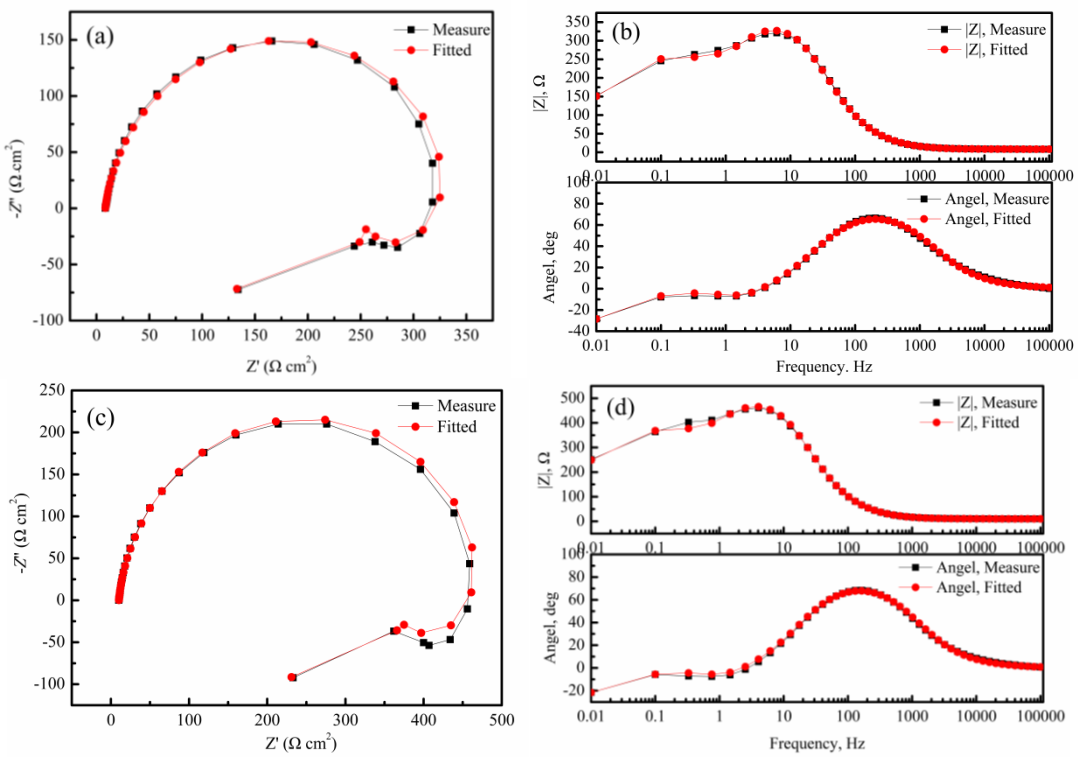


**Figure 6.** The experimental and fitted curves of EIS measurements: (a) Nyquist plots and (b) Bode magnitude (top) and phase plots (bottom) for as-cast alloy; (c) Nyquist plots and (d) Bode magnitude (top) and phase plots (bottom) for T4-treated alloy.

The impedance spectra of the GW103K alloy after T6 treatment are fitted to the equivalent circuit shown in Fig. 7. The corresponding parameters of each circuit element are listed in Table 2. $R_{sol}$ is the solution resistance, $C_{film}$ is the capacitance of the film of corrosion products and $R_{film}$ is the resistance of

film. In order to compensate for the nonuniformity of the system, a *CPE* is selected to represent the capacitance of pore ($C_{pore}$) and $R_{pore}$ is the sum of all the resistances of pore in the corrosion product, $L$ is the inductance, $R_L$ is the resistance of inductance, $C_{dl}$ is the capacitance of electric double layer locating at the interface between the bottoms of the pores, and $R_t$ is charge transfer resistance. Among them, the radii of impedance loops are affected by $R_t$, $R_{film}$ and $R_{pore}$. Therefore, the sum of $R_t + R_{film} + R_{pore}$ is used to evaluate the corrosion resistance of the alloy. According to the fitting results in Table 2, the alloy after T6-treated for 193h has the maximum sum of $R_t + R_{film} + R_{pore}$ (950.915 Ω.cm$^2$), and its corrosion resistance is the highest. Fig. 8 is the experimental impedance and fitted curves based on the fitting circuit shown in Fig. 7, the good agreement of them shows the rationality of the fitting results.

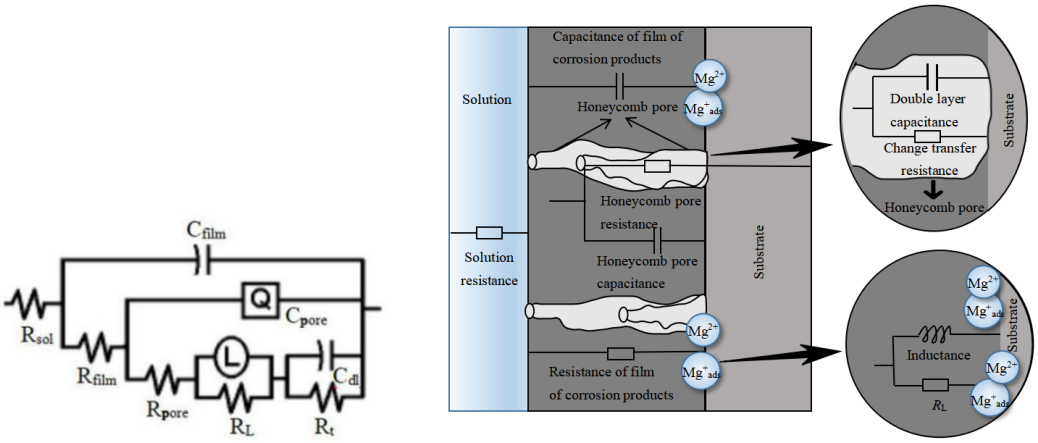


**Figure 7.** Equivalent circuit model of fitting EIS data and circuit model of physical properties of the film of corrosion products of T6-treated alloy.

**Table 2.** Fitting results of the EIS spectra of T6-treated alloys.

| Material | $R_{sol}$/ Ω.cm$^2$ | $C_{film}$/ S cm$^{-2}$ s$^{-1}$ | $R_{film}$/Ω .cm$^2$ | $CPE_{pore}$/ F.cm$^{-2}$ | $n$ | $R_{pore}$/ Ω.cm$^2$ | $L$/H | $R_L$/ Ω.cm$^2$ | $C_{dl}$/ S cm$^{-2}$ s$^{-1}$ | $R_t$/ Ω.cm$^2$ | Chsp |
|---|---|---|---|---|---|---|---|---|---|---|---|
| T6-193h | 7.952 | $1.997\cdot10^{-5}$ | 447 | $1.259\cdot10^{-2}$ | 0.6757 | 2.915 | 2.736 | 222.4 | $2.739\cdot10^{-6}$ | 501 | $5.28\cdot10^{-3}$ |
| T6-500h | 7.506 | $1.222\cdot10^{-5}$ | 4.038 | $4.33\cdot10^{-5}$ | 0.7722 | 36.28 | 1.78 | 2.977 | $1.682\cdot10^{-6}$ | 546.4 | $3.20\cdot10^{-4}$ |

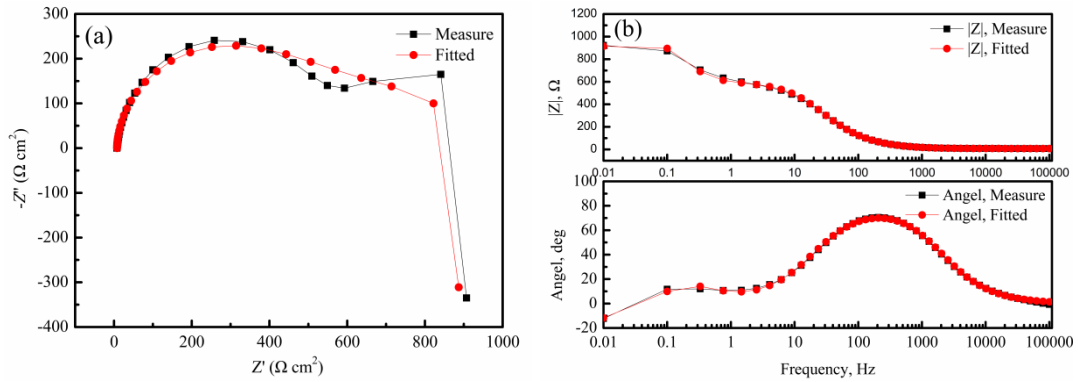

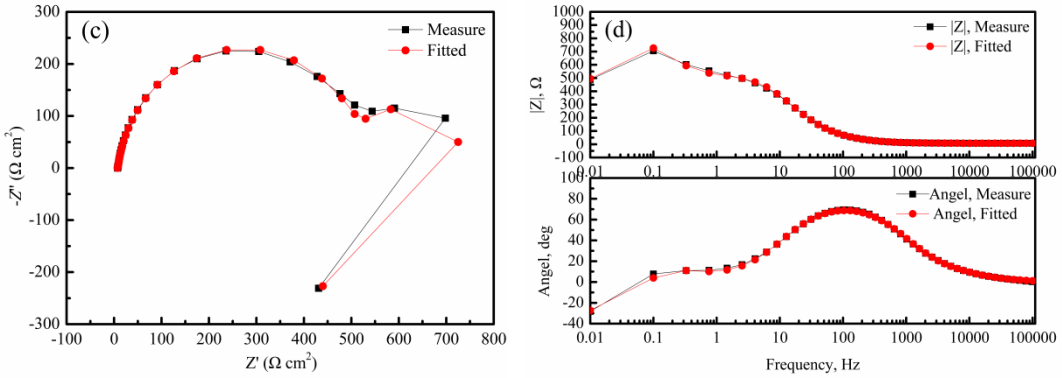


**Figure 8.** The experimental and fitted curves of EIS measurements: (a) Nyquist plots and (b) Bode magnitude (top) and phase plots (bottom) for T6-193 h alloy; (c) Nyquist plots and (d) Bode magnitude (top) and phase plots (bottom) for T6-500 h alloy.

## 4. DISCUSSION

For Mg-Gd-Y-Zr alloy, the precipitation sequence has identified as SSSS (cph)→β'' (D019) →β' (cbco)→β1(fcc)→β (bcc) [15], the metastable β' phase plays an important role for the aging hardening of the alloy [16]. However, insufficient results and even conflicting findings have been reported about corrosion behavior of the Mg-Gd-Y-Zr alloy. Peng [6] has reported the corrosion resistance of Mg-10Gd-3Y-0.4Zr alloy increases after aging treatment for 500 h, which attributes to β' precipitates formed in a type of continuous network acted as corrosion barriers. On the contrary, Chang [17] has found the increase of the β' precipitates can accelerate the corrosion in longitude direction of Mg-(6,8,10) Gd-3Y-0.4Zr. In the study of our group, the corrosion behavior of β' precipitates has been systematic investigated in three levels: atom-scale, nano-scale and global scale. We found the corrosion of β' precipitates was characterized by selective dissolution [9] and the dissolution was related to its layered structure (three layers of Mg atoms are arranged between each two RE layers), chemical dissolution occurred in RE atoms in β' precipitate because they were more active [18]. Now it has been found that the difference in the global corrosion behavior of the GW103K alloy under as-cast, solid solution and over-aging treatment conditions is related to the corrosion characteristics of $Mg_{24}(Gd,Y)_5$ phases and β' precipitates.

For the as-cast alloy, a number of $Mg_{24}(Gd,Y)_5$ phase are dispersed along the grain boundaries. The corrosion dissolution of $Mg_{24}(Gd,Y)_5$ is found in our previous studies [9]. The similar phenomena have been reported by Song et al. [14]. They have tested the relative potential difference of the second phase $Mg_{24}Y_5$ in the GW93 alloy by SKPFM and found that the potential of the matrix is nobler than that of $Mg_{24}Y_5$, and the corrosion dissolution can occur in $Mg_{24}Y_5$ phase. From Figs. 2a and b, it can be seen the localized corrosion of the as-cast alloy mainly attributes to the dissolution of the $Mg_{24}(Gd,Y)_5$, so the $Mg_{24}(Gd,Y)_5$ phase acts as anode and the surrounding matrix as cathode. Combining with Fig. 2a, Figs. 3a and b, it has been found that the corrosion products on the surface of the as-cast alloy is not compact because in that case a large amount of $Mg_{24}(Gd,Y)_5$ had been corroded. This is also the reason why the radius of high frequency capacitance loop of the as-cast alloy is the smallest compared with the other three alloys (Fig.4a). The $Mg_{24}(Gd,Y)_5$ basically dissolved after solution treatment (500 °C/4 h). Only a small amount of residual phases distributes at the grain boundaries (Fig.1b). The volume fraction

of precipitates decreases greatly, the localized corrosion of the T4-treated alloy is inhabited because the micro-galvanic coupling between the precipitate and the matrix is reduced. Compared with the as-cast alloy, the corrosion product on the surface of the T4-treated alloy is much denser (Figs. 2c and d).

It is well known, upon aging, nanoscale precipitates form and the quantity increased with increasing aging time. However, Chu et al. [19] have found that the precipitates in peak-aged WE43 have not formed a continuous network structure, so there is no corrosion barrier similar to the mechanism suggested for AZ type Mg alloys. Other aspects different from AZ type Mg alloys are the galvanic coupling effect is weak in the ZE41A T6 thixo-cast alloy [20]. In our previous studies [9,18], it has been found that the β' phase dissolves preferentially in the corrosion process and cannot act as a corrosion barrier. The volume fraction of β' phase increases while the volume fraction of $Mg_{24}(Gd,Y)_5$ decreases in the alloy after T6-treated for 193 h, and β' phase becomes the dominant factor affecting the corrosion behavior of the alloy. The corrosion pits produced by β' phase dissolution are tiny and uniform, which leads to the corrosion product on the surface more compact (Fig. 2e, Figs. 3c and 3d), improving the corrosion resistance of the alloy. When aging time reaches to 500 h, the spacing of the reticular structure of β' phase becomes wider and some of them transform for β phase ($Mg_{24}(Gd,Y)_5$). With the increase of volume fraction of $Mg_{24}(Gd,Y)_5$, the local corrosion is enhanced again, and the dispersive effect of the coarse and uneven of β' phase on the local corrosion is weakened, which decreases the corrosion resistance compared with the alloy after T6-treated for 193 h.

## 5. CONCLUSIONS

The corrosion resistance of the GW103K alloy after T6-treated for 193 h was better than that of the as-cast alloy, the solution treated alloy and T6 treated for 500 h alloy. The corrosion behavior of the alloys was associated with the corrosion characteristics of $Mg_{24}(Gd,Y)_5$ phases and β' precipitates.. $Mg_{24}(Gd,Y)_5$ phase was the main factor that influenced the corrosion behavior of the as-cast GW103K alloy, which led to localized corrosion of the alloy because of the corrosion dissolution of the $Mg_{24}(Gd,Y)_5$. After T6 treatment for 193 h, β' phase in the alloy became the dominant factor affecting the corrosion behavior. The interconnected β' phase reduced the damage of localized corrosion and improved the corrosion resistance of the alloy. After T6 treatment for 500 h, the spacing of the reticular structure of β' phase became wider and some β phase($Mg_{24}(Gd,Y)_5$) formed, which decreased the corrosion resistance comparing with the alloy after T6 treated for 193 h. The improved corrosion resistance of T6-treated for 193 h alloy was attributed to the volume fraction of β' phase increased when the volume fraction of $Mg_{24}(Gd,Y)_5$ decreased.

ACKNOWLEDGEMENT
This work was supported by the National Natural Science Foundation of China Projects under Grants No. 51961029 and the Base Construction Projects of Military-Civilian Integration.

## References

1. B. Smola, I. StulíKovÁ, J. PelcovÁ, B. L. Mordike, *J Alloys Compd.*, 378 (2004) 196.

2. H. R. J. Nodooshan, G. H. Wu, W. C. Liu, G. L. Wei, Y. L. Li, S. Zhang, *Mater Sci Eng.,* A, 651 (2016) 840
3. Q. Yang, B. L. Xiao, D. Wang, M. Y. Zheng, K. Wu, Z. Y. Ma, *J. Alloys Compd*., 581 (2013) 585.
4. I. J. Polmear, Light Alloys: Metallurgy of the Light Metals, Third editor, London: Arnold Pub., 1995.
5. C. Z. Liu, H. P. Ren, Y. Q. Song, Course of Solid State Phase Changes in Metals, Beijing: Metallurgical Industry Press, 2011.
6. L. M. Peng, J.W. Chang, X.W. Guo, A. Atrens, W. J. Ding, Y. H. Peng, *J Appl Electrochem*., 39 (2009) 913.
7. S. Q. Liang, D. K. Guan, X. Tan, *Mater. Des*., 32 (2011) 1194.
8. Q. Q. Wu, G. L. Wei, G. H. Wu, W. C. Liu, T. P. Xuan, W. J. Ding, *China Foundry*, 13 (2016) 276.
9. S. Yu, R. L. Jia, T. Zhang, F. H. Wang, J. Hou, H. X. Zhang, *Acta Metall. Sin*., 32 (2019) 433.
10. C. N. Cao, J. Q. Zhang, An introduction to Electrochemical Impedance Spectroscopy, Beijing: Science Press, 2002.
11. R. Arrabal, A. Pardo, M. C. Merino, M. Mohedano, P. Casajús, K. Paucar, G. Garces, *Corros. Sci.,* 55(2012) 301.
12. M. I. Jamesh, G. S. Wu, Y. Zhao, D. R. McKenzie, M.M.M. Bilek, P. K.Chu, *Corros. Sci*., 91 (2015) 160.
13. X. B. Liu, D. Y. Shan, Y. W. Song, E. H. Han, *J Magnes. Alloy*, 5 (2017) 26.
14. Y. W. Song, D. Y. Shan, E. H. Han, *J. Mater. Sci. Technol*., 9 (2017) 50.
15. S. M. He, X. Q. Zeng, L. M.Peng, X. Gao, J. F. Nie, W. J. Ding, *J Alloys Compd*., 421 (2006) 309.
16. J. X. Zheng, L. D. Tan, X. S. Xu, R. C. Luo, B. Chen, *Mater. Charact.*, 117 (2016) 76.
17. J. W. Chang, X.W. Guo, S. M. He, P. H. Fu, L. M. Peng, W. J. Ding. *Corros. Sci*., 50 (2008) 166.
18. S. Yu, R. L. Jia, F. Guo, T. Zhang, F. H. Wang, *Mater. Lett.*, 257 (2019):126680.
19. P. W. Chu, E. A. Marquis, *Corros. Sci*., 101 (2015) 94.
20. Z. Szklarz, M. Bisztyga, H. Krawiec, L.L.Dobrzyñska, L. Rogal, *Appl. Surf. Sci.*, 405 (2017) 529